Article

Not peer-reviewed version

Damage Identification in a Helicopter Rotor Blade Root in Realistic Load Conditions With Neural Network-Based Algorithms

Pietro Ballarin * , Giuseppe Sala , Marco Macchi , Irene Roda , Andrea Baldi , Alessandro Airoldi

Posted Date: 10 June 2024

doi: 10.20944/preprints202406.0421.v1

Keywords: fiber bragg grating sensors; structural health monitoring; artificial neural network; composite structure; rotor blade; load monitoring

Article

Damage Identification in a Helicopter Rotor Blade Root in Realistic Load Conditions with Neural Network-Based Algorithms

Pietro Ballarin [1,*], Giuseppe Sala [1], Marco Macchi [2], Irene Roda [2], Andrea Baldi [3] and Alessandro Airoldi [1]

[1] Department of Aerospace Science and Technology, Politecnico di Milano, Milan, 20156 (MI), Italy; giuseppe.sala@polimi.it, alessandro.airoldi@polimi.it
[2] Department of Management Engineering, Politecnico di Milano, Milan, 20156 (MI), Italy; marco.macchi@polimi.it, irene.roda@polimi.it,
[3] Leonardo Helicopters Division, Cascina Costa di Samarate, 21017 (VA), Italy; andrea.baldi01@leonardo.com
* Correspondence: pietro.ballarin@polimi.it;

Abstract: Monitoring the integrity of aeronautical structures is fundamental for safety. Structural Health Monitoring Systems (SHMS) perform real-time monitoring functions, but their performances must be carefully assessed. In this work the damage detection performances of a strain-based SHMS, were evaluated on a composite helicopter rotor blade root. The SHMS monitored the bonding between the central core and the surrounding antitorsional layer. A damage detection algorithm was trained through Finite Element analyses performed on the component. The effects of the loads variability and of damages was decoupled by including a load recognition step in the algorithm. Load recognition was accomplished in different ways: version#1 adopted an Artificial Neural Network (ANN) trained on blades in pristine condition; version#2 was trained also on damaged blades; version#3 adopted a calibration matrix method. Anomaly detection, damage assessment, and localization were performed by using an ANN. Results showed a higher load identification and anomaly detection accuracy for version#1 and version#2 compared to version#3. Gaussian noise reduced anomaly detection and damage assessment performances, and reduced damage localization accuracy for bigger damages. The damage detection performance were obtained for a fibre optic based-SHMS, including the trade-off between probability of detection and false alarm rate for different damage sizes.

Keywords: fiber bragg grating sensors; structural health monitoring; artificial neural network; composite structure; rotor blade; load monitoring;

---

1. Introduction

Composite materials are widely used in the aerospace field since they exhibit good performances in terms of high strength, stiffness and low density. Optimal fatigue performance in tension and the possibility of producing large monolithic parts without junctions represent other appealing aspects motivating the adoption of composite materials for primary structural parts. Composite structures usually require complex manufacturing procedures and a high manpower. The complexity of such manufacturing processes can give raise to manufacturing defects [1-3], which can propagate in the structure during the operational life [4-6] affecting the structural properties. Defects can be related to both fibres and matrix. In the first case the instability of the fibres creates wrinkles during the lamination phase [7-8]. In the second case voids can nucleate in the matrix during the curing cycle or can be trapped during the lamination [9-10]. Bondings are also subjected to manufacturing defects like porosity [11], but also faulty curing, contamination with release agents, de-icing fluid or fingerprints can occur [12]. Such defects affect properties like adhesive strength and toughness up to a degradation below 50% [13-14]. In some cases it can happen that during the polymerization no chemical interaction occurs between the adhesive and the bonded surfaces: this is known as kissing bond and in this case conventional Non Destructive Techniques (NDT) cannot detect these defects because material continuity is guaranteed. Measurement of local vibration non-linearity and acoustic microscopy demonstrated good detection performances [15-16] at this purpose. NDT can help detecting defects or damages inside composite components [17-19] but they have some drawbacks. First they are able to inspect the structure only locally and second, usually the component must be disassembled from the aircraft's structure to be inspected increasing the aircraft's downtime with the consequent loss of revenue. Structural Health Monitoring Systems (SHMS), differently from NDT, provide an on-line inspection of the structure without the need to disassemble structural components and they are able to monitor the structure on a more diffused area [20]. Nowadays different types of SHMS are studied, such as the ones based on piezoelectric wafer active sensors, piezoresitive sensors, Fibre Bragg-Grating (FBG) sensors and the ones based on comparative vacuum [21-23]. Overall, FBG-based SHMS seem to be particularly promising for the monitoring of composite structures as they can be embedded and protected inside composite laminates [24], and the sensors can be used to monitor the curing cycle [25]. Moreover they are not affected by electromagnetic disturbances and they are characterized by a reduced weight [26-29]. Many studies were presented in literature regarding the implementation of SHMS using machine-learning tools [30]. For instance in [31] the authors identified a damaged welded structure adopting an Artificial Neural Network (ANN) simulating a pristine lamb wave signal, which was compared with the measured signal to detect the damage. In [32-33] the performances of a SHMS based on an ANN for damage detection were evaluated in a metallic helicopter stiffened panel. In [34] a methodology for damage detection in aerospace structures based on Gaussian process was proposed. In [35, 36] a methodology for damage detection under variable loads was presented and applied to a UAV composite wing. In [37] the Convolutional Neural Networks (CNN) were adopted for damage detection in the same type of structure.

The above mentioned criticalities regarding the adhesive bondings and the potential of the machine learning techniques motivated the study presented in this work. In this paper the performances of a SHMS based on FBG sensors were evaluated in an adhesive layer of a composite helicopter rotor blade root. This type of element represents a critical sub-component of the blade, as it shows a high manufacturing complexity, which increase the probability to include manufacturing defects. An experimentally validated Finite Element (FE) model of the component was exploited to train an ANN-based algorithm. Three versions of the algorithm were proposed with the aim to detect damages in the adhesive layer joining the central core and the external anti-torsional layer of the blade root. These versions adopted different strategies to recognize the applied loads: such step was needed to uncouple the variability in the strain field due to damages from the one inherent to the variation of the applied loads. This work was divided in four parts: in section 2 the component under analysis was described as well as its modelling with FE and model validation, in section 3 the three versions of damage detection algorithm were presented together with the methodology for the creation of the dataset to train the ANN, in section 4 the performances of the three versions of the algorithm were investigated under different levels of noise, finally in section 5 conclusions and main findings were discussed.

2. Finite Element Model Description and Model Validation

2.1. Finite Element Model of the Blade Root

The component was represented by a composite helicopter rotor blade root, which is shown in Figure 1a and b and was characterized by a composite central core that was wrapped by an anti-torsional layer, the former coloured in light green in Figure 1a. The cross section is shown in detail in Figure 1c. The lamination sequence of the composite rotor blade root cannot be disclosed for confidentiality reasons. Three passing through holes were positioned in the curved part of the blade root; one of them was located in the symmetry centre and the other two were located symmetrically to the central one.

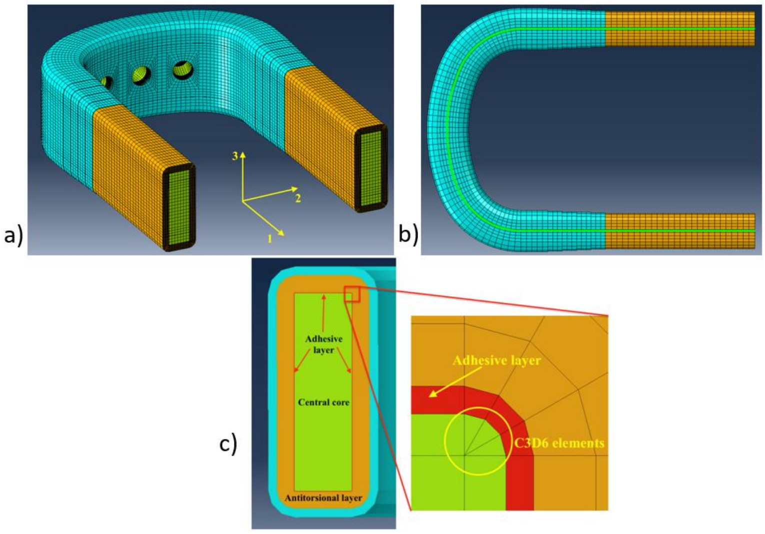

Figure 1. a) blade root; b) curvilinear path of the central core; c) cross section with detail of the mesh of the corner region with C3D6 type elements.

In correspondence of the curved part, additional layers of composite plies were co-bonded over the anti-torsional layer: such plies produced a tapering in the cross-section, which is clearly visible in Figure 1a.

The anti-torsional layer was connected to the central core by means of an adhesive layer, which is depicted in Figure 1c, and represents the focus of this work, since the SHMS was aimed at monitoring its structural integrity. Referring to Figure 1, the following colours were used to distinguish the main subcomponents: colour light green was used for the central core, colour orange was used for the anti-torsional layer, colour light blue was used for the tapered anti-torsional layer, and colour red was used for the adhesive layer.

The component was modelled with the software Simulia/Abaqus and the input file was automatically generated through a Matlab® script. In Figure 1 the mesh adopted for the component is shown evidencing the three types of elements that were adopted: hexahedral bricks, wedge elements, and cohesive elements (respectively types C3D8, C3D6, and COH3D8 in the solver code [38]). The anti-torsional layer and the tapered anti-torsional layer were modelled ply by ply, with C3D8 type elements to well capture the state of stress. The central core was modelled with both C3D8 and C3D6 type elements. As it can be seen in Figure 1c, the C3D6 type elements were used only in the corners of the central core in order to allow meshing properly the fillet region, while in all the other locations C3D8 type elements were adopted. The adhesive layer was modelled with cohesive elements COH3D8 type having a thickness of 0.1 mm. Their penalty stiffness was set equal to the value calculated according to [39], considering, as the adherent thickness t, the thickness of the anti-torsional layer. Eq. 1 related the penalty stiffness of the cohesive element to the out-of-plane stiffness and thickness of the adjacent layers:

$$K = \alpha \frac{E_{33}}{t} \quad (1)$$

where K represented the normal penalty stiffness of the cohesive element, α represented a constant which was set equal to 50 according to [39]. E_{33} represented the normal out-of-plane modulus of the anti-torsional layer. A total of 16 elements were used to mesh the anti-torsional layer through the thickness, while for the central core 7 elements were used along the cross section width and 24 elements were used in the height of the cross section. For the anti-torsional tapered layer, a total of 5 elements were adopted through its thickness. A characteristic element length of 3 mm along the curvilinear path was adopted.

2.2. Integration of Finite Element Model into Full Scale Blade Model and Validation with Experimental Data

The model of the component was introduced into a model representing the blade subjected to a fatigue test that was actually performed on a test rig; all the components are shown in Figure 2a and are listed below:

- Blade root: representing the component to be monitored. Its meshing strategy was presented in the previous subsection;

- Blade: representing the part of the blade from the end of the blade root up to about half of the whole blade. The blade was modelled using C3D8I type elements having a a characteristic length of 5 mm;

- Tabs: these elements were bonded to the blade and were needed to transfer the load to the blade root. Tabs were modelled with C3D10 type elements having a characteristic length of 10 mm;

- Bearing: metallic element, which was representative of the connection of the blade to the hub, such connection was implemented by three bolts passing through the holes of the blade root. The bearing was modelled with C3D8R type elements having characteristic length of 2.5 mm;

- Pitch arm: a metallic element that was bonded to the blade root and allows introducing loads to rotate the blade about pitch axis. The pitch arm was modelled with C3D10 type elements having a characteristic length equal to 5.5 mm;

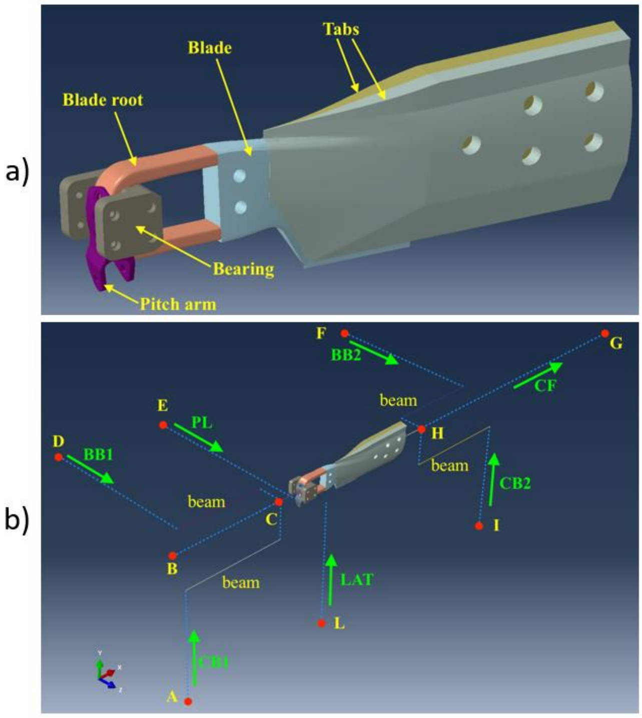

Figure 2. a) Full blade, b) full test rig assembly.

A non-linear static FE model was developed in which the blade root was connected to the rest of the blade with a tie interaction; the surfaces involved in such interaction are shown in Figure 3, highlighted in red colour. Tabs were also connected to the blade with a tie interaction, as well as the pitch arm to the blade root. A contact interaction between the blade root and the bearing was modelled introducing a friction coefficient equal to 0.1. The loads exerted by the actuators in the fatigue tests were applied in the model through connector elements type CONN3D2 [38] and are shown in Figure 2b, namely:

- CF: centrifugal force;
- PL: force acting on the pitch link, which counterbalances the pitching moment;
- LAT: lateral load, which is given by the lag damper connected to the blade;
- CB1 and CB2: in-plane loads;
- BB1 and BB2: out-of-plane loads;

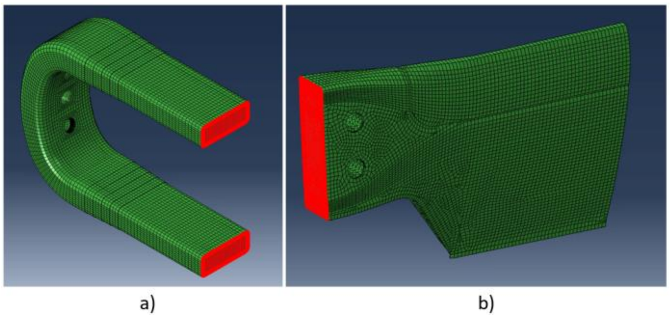

Figure 3. surfaces involved in the tie connection between the blade root a) and the rest of the blade b), surfaces are highlighted in red colour.

Table 1 describes the constraints applied to the structure, most of them consisting of spherical hinges.

Table 1. constrained degrees of freedom referred to nodes A to L of Figure 2b: 1-3 translations in axis x,y,z, 4-6 rotations about axis x,y,z.

A	B	C	D	E	F	G	H	I	L
1,2,3	1,2,3	2,3	1,2,3	1,2,3	1,2,3	2,3	2,3,4	1,2,3	1,2,3

The analysis was performed in two steps: in step 1 a preloading of the bolts was performed, as to establish the contact between the blade root and the bearing, while in step 2 the external loads were applied to the blade. The load set applied, both in the experiment and in the model, was representative of the forces applied to the blade during its operational life.

The model was validated experimentally comparing the strain values acquired from the strain gauges positioned on the straight arms of the blade root, the picture of the test setup with the strain gauges can be observed in Figure 4.

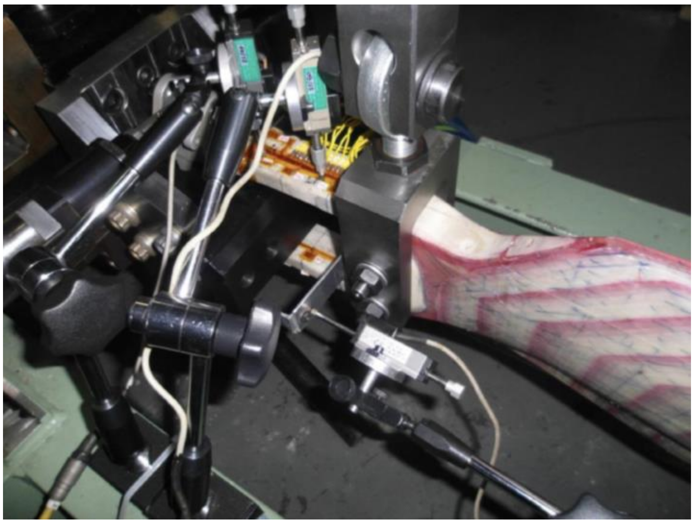

Figure 4. blade root subjected to testing in a test rig, and strain gauges positioned in correspondence of the straight arms of the blade root.

The results of the validation of the non-linear implicit model are presented in the second column of Table 2, and they were normalized with respect to the strain gauge number S7 for confidentiality reasons. Strain values were extracted from the FE model in the centroid position of the elements located on the surface, in correspondence of the position of the strain gauges in the experimental set-up.

doi:10.20944/preprints202406.0421.v1

Table 2. Finite Element model validation with experimental data.

Strain gauge code	Non-linear implicit model	Linear model
	Difference % 100×(Test values – FEM strain values)/Test value S7	**Difference %** 100×(Test values – FEM strain values)/ Test value S7
S1	-26.27%	13.77%
S2	-1.67%	15.95%
S3	-3.08%	-4.82%
S4	-2.05%	-11.70%
S5	0.17%	-8.47%
S6	12.2%	27.42%
S7	10.46%	39.62%
S8	-14.03%	21.46%
S9	3.33%	6.23%
S10	-4.38%	10.99%
S11	20.46%	16.83%
S12	5.28%	20.99%
S13	8.93%	31.04%
S14	-1.19%	13.88%

Considering the complexity of the component, the possible manufacturing defects, geometrical imperfections and alignment imperfections in the tests, the pointwise correlation between the numerical and the experimental strains can be evaluated as acceptable.

However, the scope of the model involve the accomplishment of a large number of analyses in order to train and test the ANN that was used for damage and load detection. For this reason it was deemed of primary importance to reduce the computational cost. Consequently the model was adapted to perform linear analyses. A linear model was created starting from the nonlinear one and removing the contact interactions. In particular, the contact between the blade root and the bearing was removed and replaced with a tie interaction. However, it was observed that the relative tangential motion that occurred in the presence of the contact helped reducing the shear stresses transmitted from the blade to the bearing. A better representation of the real working condition was accomplished by using a layer of cohesive elements (COH3D8 [38]) with a very low shear penalty stiffness (70 N/mm3) so to reduce the transmitted shear stresses, as it occurs in the case of a contact interaction. The cohesive elements were interposed between the bearing and the blade. The normal penalty stiffness was set equal to the value adopted for the adhesive interface.

The results of the linear model validation are shown in third column of Table 2. As it can be observed a not negligible mismatch was obtained between the linear model and the non-linear one. The percentage errors with respect to the experiments are higher for the linear model. However, since the scope of this paper was an evaluation of the performances of a SHMS applied to a real-world thick composite element, with complex geometrical features and in combined load conditions, the linear model was considered an acceptable approximation of a real blade root. Indeed, for a real application, a more detailed model identification has to be performed to make available a high/fidelity model capable of correctly predicting the strain field evolution due to load variation and damage occurrence, so to adopt it in the training phase of the ANN algorithm development. Modern high-performance computing can certainly provide the resources for the application of the method to fully non linear model.

3. Damage Detection Algorithm and Virtual SHMS Description

Damage detection procedure was characterized by three main steps [40]: anomaly detection, whose task was to detect the presence of damage, damage assessment, whose task was to provide an estimation of damage size and damage localization, which provided the information about the location of the damage on the component.

The main problem related to this specific application was that the strain field was affected by the presence of damage and by the application of the load. In order to detect a possible presence of damage these two aspects were decoupled. Three versions of the algorithm were evaluated and compared considering the noise sensitivity and the damage detection performances. In this study, the SHMS was represented by virtual sensors, represented by elements of the FE model, and the strain was obtained by sampling the strain values from the element located on the optical fibre path. For this study the machine learning toolbox of Matlab® was adopted.

3.1. Damage Detection Algorithms

The basic strategy for damage detection was based on decoupling the effects of the load application from the effects of the damage by first identifying the applied load set and subsequently identifying the possible presence of damage. The assumption behind such strategy was that the load set could be recognized with a satisfactory accuracy despite the perturbation that the damage created to the strain field. This assumption was verified in the next section.

The three versions of the algorithm differed only in the first stage, which was the load identification step. In version #1, the load identification was performed with the ANN trained only on FE analyses of the blade in pristine configurations, while in version #2, the load identification was performed with the ANN trained on FE analyses of the blade in pristine and damaged configuration. In both version #1 and version #2, the identification of the load was performed using an ANN for regression. The architecture of this ANN, hereafter named as ANN1, was characterized by 3 layers, each one composed of 10 neurons. 70% of the dataset was used for the training, 15% for validation, and the remaining 15% for testing. More details about the architecture are reported in Table 3.

Table 3. Artificial Neural Network architecture for ANN 1.

Type	Node number per layer	Number of hidden layers	Training function	Dataset partition [Training/validation/test]	Activation function
Regression	10	3	Levenberg-Marquardt backpropagation	[70/15/15]	Hyperbolic tangent sigmoid

The ANN1 took in input the strain values of the sensors and provided in output the identified load set. In version #3, the load identification was performed by finding the load set from the strain measures inverting the calibration matrix. Actually, the solution of such problem for the load set is known to be particularly affected by the bad conditioning of the system [41]. The load identification, assuming a linear response of the model, was based on Eq. 2, which related the vector of the applied load set to the strain values acquired at the sensor position:

$$\{\varepsilon\} = [K]\{P\} \qquad (2)$$

where $\{\varepsilon\}$ represented the vector containing the strain values of each sensor; its size was equal to the number of sensors by 1. $[K]$ represented the calibration matrix obtained by the FE model with size equal to number of sensors by number of load components. $\{P\}$ represented the load vector with size equal to number of load components by 1. In this case study, the number of load components was equal to 7. Consistently with the assumption of negligible effect of damage on the overall strain field involved in load identification, the calibration matrix $[K]$ was calculated on the blade in pristine condition. The load set was then identified computing the pseudo-inverse of the calibration matrix, presented in Eq. 3.

$$\{P\} = ([K]^T[K])^{-1}[K]^T\{\varepsilon\} \quad (3)$$

where $\{P\}$ represented the load set to be identified, and $[K]^T$ represented the transposed of the calibration matrix $[K]$. Table 4 shows a summary of the load identification methodologies for all the three versions of the algorithm.

Table 4. load identification methodologies for the three versions of the algorithm.

Algorithm version	Load Identification Methodology
Version #1	ANN trained only on blade in pristine conditions
Version #2	ANN trained on blade both in pristine and damaged conditions
Version #3	Solution of inverse problem finding load set $\{P\}$ using Eq. 3

Once the load set was identified, regardless of the algorithm's version, Eq. 2 was used to calculate the nominal strain values that would be provided by the sensors for the identified load condition with the blade in pristine condition. Such passage represented a simplification allowed by the linearity of the model. If the non-linear model had to be considered the architecture of the damage detection process would not change, but the strains should have been evaluated through a non-linear analysis performed with the identified load set. By comparing the calculated strain on the notional model and the actual strain read by the sensors it was possible to define a damage index for each sensor representative of the structural integrity of the blade; the proposed damage index was reported in Eq. 4.

$$damage\ index_i = \left(\varepsilon_i^{calculated} - \varepsilon_i^{measured}\right)^2 \qquad (4)$$

Where $\varepsilon_i^{calculated}$ represented the strain value of the i^{th} sensor calculated using Eq. 2, while $\varepsilon_i^{measured}$ represented the strain value measured by the sensor. An ANN for pattern recognition was then adopted to detect the presence of damage based on the damage indexes previously calculated, the ANN took in input the vector of damage indexes and provided a scalar output which was compared to a threshold value. The blade was considered damaged if such output exceeded a predefined threshold. If damage was detected the next step of the algorithm was related to the identification of the damage dimension and its location [**40**], to perform such task an ANN for regression was adopted.

All the versions of the algorithm were trained, validated and tested adding a Gaussian noise with zero mean and standard deviation equal to 1%, 2%, 4% and 6% of the nominal strain value provided by the sensor (in this case from the strain sampled from the FE model). For all the versions of the algorithm the anomaly detection was performed with an ANN for pattern recognition, hereafter named *ANN 2*, whose architecture is described in **Error! Reference source not found.**. Damage assessment and localization were performed with an ANN for regression, hereafter named *ANN 3*, whose architecture is described in **Error! Reference source not found.**. *ANN 3* took in input the damage index pattern and the output was represented by the damage size and location. Regarding *ANN 2* and *ANN 3*, 70% of the dataset was used for the training, 15% for validation, and the remaining 15% for testing.

Table 5. Artificial Neural Network architecture for *ANN 2*.

Type	**Node number per layer**	**Number of hidden layers**	**Training function**	**Dataset partition** [Training/validation/test]	**Activation function**
Pattern recognition	10	3	Levenberg-Marquardt backpropagation	[70/15/15]	Hyperbolic tangent sigmoid

Table 6. Artificial Neural Network architecture for *ANN 3*.

Type	**Node number per layer**	**Number of hidden layers**	**Training function**	**Dataset partition** [Training/validation/test]	**Activation function**
Regression	10	2	Levenberg-Marquardt backpropagation	[70/15/15]	Hyperbolic tangent sigmoid

The architecture for each ANN was chosen based on preliminary studies aimed at identifying the configuration providing a better quality of the results, this operation led to use a number of three hidden layers for ANN 1 and ANN 2 and two hidden layers for ANN 3. The flow diagrams of the damage identification algorithm are presented in Figure 5 for each of the algorithm's versions. In this case Figure 5a refers to both version #1 and version #2 since the only difference between them was related to the condition of the blade on which the ANN 1 was trained.

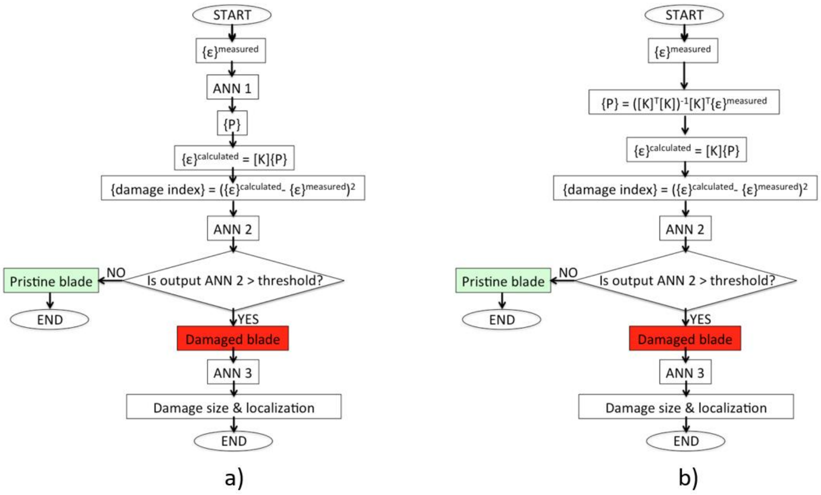

Figure 5. a) Damage detection algorithm diagram for version #1 and version #2; b) damage detection algorithm diagram for version #3.

3.2. Virtual SHMS for Strain Acquisition

A virtual sensing system was considered embedded in the blade root, based on FBG sensors carried by optical fibres. A total of 6 virtual optical lines were supposed to monitor the component with the paths shown in Figure 6a, while in Figure 6b an example of optical fibre sensors integrated in a composite helicopter tail rotor blade can be observed. One element was treated as one FBG sensor since the characteristic length of the elements, about 3 mm, was comparable to the possible length of a real FBG sensor. By taking the strains at the centroid of the element, the virtual strain could be considered a measure of the average strain in the FBG located in the correspondent position. The optical fibre paths were considered located inside the anti-torsional layer, at a distance of 0.25 mm from the adhesive layer. Strain values in a prescribed set of elements along the optical fibre path were obtained rotating the entire strain tensor of 45° and considering only the strain component directed along the optical fibre path ε_{11} of the rotated tensor.

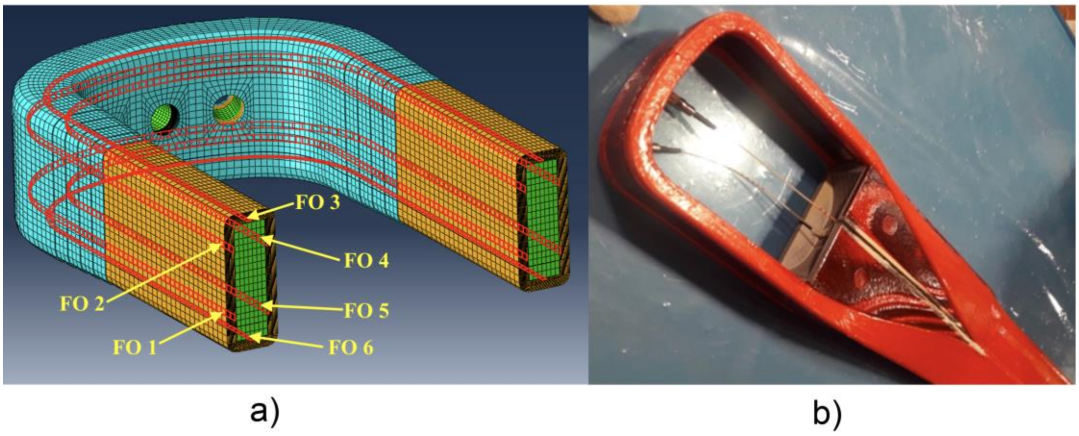

Figure 6. a) virtual optical fibre paths; b) example of optical fibres integrated in a helicopter tail rotor blade, adapted from [42] with permission.

A number of 10 virtual FBG sensors per optical fibre was considered, consistently with the limitations provided by the multiplexing technique [43], so that a total of 60 FBG's were employed in the SHMS. Sensors were distributed equally spaced along each optical fibre with a pitch equal to 42 mm.

3.3. Dataset Creation and Training

The most important interfaces in the blade root were the ones represented by the adhesive joints. These were critical because they were obtained through secondary bonding or co-bonding process, involving parts that have been already cured. It was exactly for this reason that attention was focused on such interfaces simulating damages that could be originated during manufacturing, which can propagate during the operational life of the helicopter.

To create datasets to train and test the ANNs different FE analyses were performed introducing damages during the generation of the input file deleting the cohesive elements included in a space described by a sphere located on the surface of the adhesive layer to be monitored. Such damages were introduced in 40 different locations on the adhesive, in detail, referring to Figure 7a, damages were introduced in 4 locations equally spaced along the cross section coordinate and 10 locations equally-spaced along the curvilinear path. Only one damage per FE analysis was created in the adhesive. Table 7 shows the coordinate values referred to the coordinate system shown in Figure 7a where the damages were introduced: it must be specified that for each combination of curvilinear path coordinate and cross section coordinate 9 damage dimensions were analysed in the range from 3 mm to 30 mm. Being the cross section coordinate a closed path, 0% corresponded to 100% of the coordinate value, thus in this work the maximum value was set to 75%. A total 360 damage scenarios were considered in this study, resulting by the combination of 10 damage locations in the curvilinear path coordinate, 4 damage location in the cross section coordinate and 9 damage dimensions.

Table 7. coordinate values at which damages were introduced in the adhesive layer and corresponding damage dimension in mm.

		Curvilinear path coordinate %									
		0	**11.11**	**22.22**	**33.33**	**44.44**	**55.55**	**66.66**	**77.77**	**88.88**	**100**
Cross section coordinate %	**0**	3-6-9-12-15-18-21-24-30	3-6-9-12-15-18-21-24-30	3-6-9-12-15-18-21-24-30	3-6-9-12-15-18-21-24-30	3-6-9-12-15-18-21-24-30	3-6-9-12-15-18-21-24-30	3-6-9-12-15-18-21-24-30	3-6-9-12-15-18-21-24-30	3-6-9-12-15-18-21-24-30	3-6-9-12-15-18-21-24-30
	25	3-6-9-12-15-18-21-24-30	3-6-9-12-15-18-21-24-30	3-6-9-12-15-18-21-24-30	3-6-9-12-15-18-21-24-30	3-6-9-12-15-18-21-24-30	3-6-9-12-15-18-21-24-30	3-6-9-12-15-18-21-24-30	3-6-9-12-15-18-21-24-30	3-6-9-12-15-18-21-24-30	3-6-9-12-15-18-21-24-30
	50	3-6-9-12-15-18-21-24-30	3-6-9-12-15-18-21-24-30	3-6-9-12-15-18-21-24-30	3-6-9-12-15-18-21-24-30	3-6-9-12-15-18-21-24-30	3-6-9-12-15-18-21-24-30	3-6-9-12-15-18-21-24-30	3-6-9-12-15-18-21-24-30	3-6-9-12-15-18-21-24-30	3-6-9-12-15-18-21-24-30
	75	3-6-9-12-15-18-21-24-30	3-6-9-12-15-18-21-24-30	3-6-9-12-15-18-21-24-30	3-6-9-12-15-18-21-24-30	3-6-9-12-15-18-21-24-30	3-6-9-12-15-18-21-24-30	3-6-9-12-15-18-21-24-30	3-6-9-12-15-18-21-24-30	3-6-9-12-15-18-21-24-30	3-6-9-12-15-18-21-24-30

Figure 7a andREF Figure _Ref153980827b show an example of a damage of 30 mm of diameter located at 44.44 % of the curvilinear path and at 50% of the cross section coordinate.

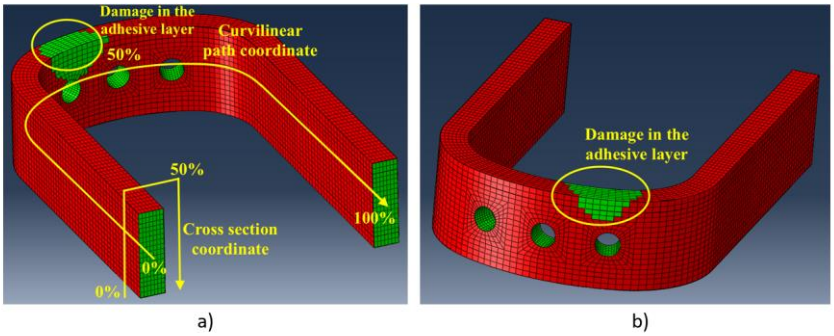

Figure 7. a) Coordinate system for damage introduction and example of damage of diameter 30 mm located at 44.44% of the curvilinear path and 50% of the cross-section coordinate, better shown in b).

To create a dataset considering different load conditions and to limit the number of FE analyses to be performed the linearity of the FE model was exploited. A calibration matrix was calculated for each damage size and position performing a FE analysis applying 1 unitary load per time. Once the calibration matrices were obtained (each one specific for damage size and position), different strain fields were obtained multiplying the calibration matrix by the load condition, representative of the operational loads. Two load sets were considered, hereafter named as load set A and load set B, each one varying in time according to the following laws, represented in Eq. 5 and Eq. 6 for Load set A and load set B respectively.

$$\begin{cases} CF = 122.27 \\ BB1 = 0.67 + 0.33 \sin \omega t \\ CB1 = 6.1 + 1.4 \sin \omega t \\ LAT = 8.89 + 3.33 \sin \omega t \\ PL = 2.22 + 1.11 \sin \omega t \\ BB2 = 0.67 + 0.33 \sin \omega t \\ CB2 = -6.11 - 1.55 \sin \omega t \end{cases} \quad (5)$$

$$\begin{cases} CF = 106.24 + 106.24 \sin \omega t \\ BB1 = 0.88 + 0.88 \sin \omega t \\ CB1 = 6.66 + 6.66 \sin \omega t \\ LAT = 8.89 + 8.89 \sin \omega t \\ PL = 2 + 2 \sin \omega t \\ BB2 = 0.88 + 0.88 \sin \omega t \\ CB2 = -7.22 - 7.22 \sin \omega t \end{cases} \quad (6)$$

Where ω represented the circular frequency and t represented the time. CF, BB1, CB1, LAT, PL, BB2, and CB2 represented the load components presented in Figure 2b.

The former equations were normalized with respect to the maximum peak value of BB1 of load set A for confidentiality reasons. Different load conditions were created evaluating Eq. 5 and Eq. 6 in 100 time intervals for each one in their period, obtaining a total of 200 load conditions.

For the stage of load identification, in version #1, the training of ANN1 was performed on the 70% of a dataset made of 8000 load conditions, obtained repeating 40 times the 200 load conditions adding a Gaussian noise. Considering the dataset for the ANN1 of version #2, the same number of load conditions for pristine and damaged were considered, each one composed by 8000 load conditions. The input of ANN1 was represented by the strain acquired at sensor location and the output was represented by the identified load set.

Considering the dataset for the ANN2, the latter was equally divided in two subsets, one of them was characterised by only pristine conditions and the other one was characterized only by damaged conditions, obtaining a balanced dataset, as suggested in [33]. Each of the 200 load conditions was combined with the 360 damage scenarios, obtaining a dataset made of 72000 damage index pattern, the same number was then produced with the blade in pristine condition repeating each load condition 360 times adding a Gaussian noise and calculating the related damage index pattern. The input of ANN2 was represented by the damage indexes calculated for each sensor, according to Eq. 4, and the output was represented by a scalar value between 0 and 1, the blade was then classified pristine or damaged depending on the chosen threshold value.

Considering ANN3 the related dataset was made only of damage conditions, therefore, only the part of the dataset of ANN2 related to the damaged conditions was used to train and test ANN3. The input of ANN3 was characterized by the damage index pattern, as it was done for ANN2, and the output was represented by the position and the damage size estimated.

4. Results

In this section the results of all the algorithm versions are presented in terms of load identification, anomaly detection, damage assessment and localization. The performances of all the versions of the algorithm were evaluated for different noise levels, namely 1%, 2%, 4%, and 6%. Since dataset was divided randomly for training, validation and testing, in order to obtain a more reliable estimation of the performance of the algorithm’s results were averaged on 10 algorithm's runs.

4.1. Load Identification

Results about load identification for algorithm version #1 and version #2 are provided in Figure 8, in which the average error was calculated for each load component, moreover, a comparison between the identified loads on the pristine and damaged blade is shown. The error was normalized with respect to the maximum magnitude of each load component.

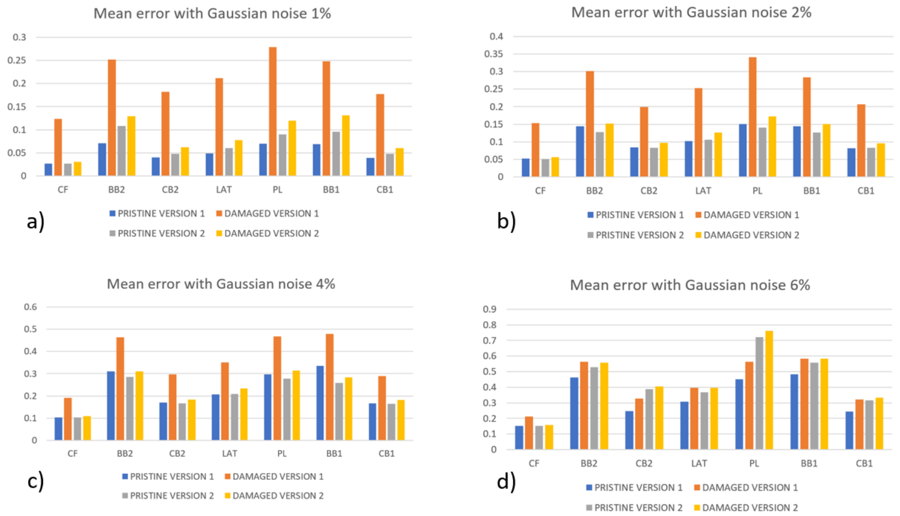

Figure 8. Mean percentage error on load identification referred to algorithm version #1 and version #2 for a) 1% Gaussian noise, b) 2% Gaussian noise, c) 4% Gaussian noise and d) 6% Gaussian noise.

As expected, the error for all the load components increased as the noise level increased. For example an increase in the maximum mean error of 0.27% for PL load component with 1% noise level to a maximum average error of 0.76% for the same load component with a noise level of 6% was obtained. It can be observed that in all the cases the error related to the damaged conditions was higher with respect the one obtained for pristine condition, but this difference decreased when the noise level increased: a possible explanation for this behaviour could be to consider the damage like a perturbation to the strain field, which is similar to the effect of the noise, so as the noise level increased it tended to cover the effect of the damage. For what concerns the comparison between the algorithm's versions it can be observed that version #1 of the algorithm provided a higher difference between errors in pristine and damaged condition with respect to version #2, however, such difference decreased by increasing the noise level.

In Figure 9 the mean percentage error on load set identification for version #3 of the algorithm is shown, as already mentioned loads were obtained solving for the load set {P}, as in Eq. 3. Errors related to the load components CB2 and LAT were not reported because off-scale for the plot: the error is 5 to 20 times the maximum magnitude of the loads, anyway, their contribution to the strain field it was verified to be one order of magnitude lower than the other loads acting on the blade, this may be the reason for such a high error.

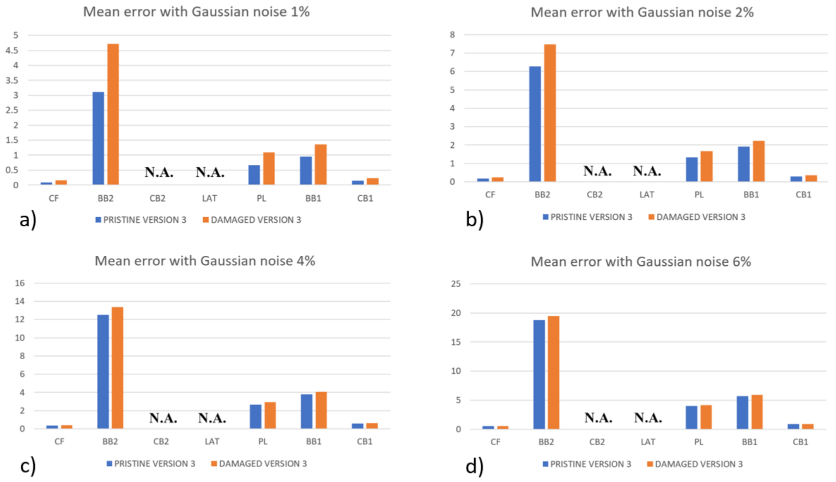

Figure 9. Mean percentage error on load identification referred to algorithm version #3 for a) 1% Gaussian noise, b) 2% Gaussian noise, c) 4% Gaussian noise and d) 6% Gaussian noise. Load components CB2 and LAT are not reported because off-scale.

Preprints.org (www.preprints.org) | NOT PEER-REVIEWED | Posted: 10 June 2024 doi:10.20944/preprints202406.0421.v1

The same behaviour for version #1 and version #2 of the algorithm was observed. By increasing the noise level the error increased as well, moreover, for all the noise levels and for all the load components the damaged configuration provided higher errors. It was interesting to observe that also in this case, by increasing the level of noise, the difference between the error in pristine and damaged conditions reduced. However, the load identification method of version #3 provided worse results with respect to version #1 and version #2 of the algorithm: the load set identification by means of the ANN 1 revealed much more effective with respect to solve the inverse problem for the load set {P}, as in Eq. 3.

4.2. Anomaly Detection

The performances of the algorithm to detect a possible presence of damage were evaluated considering the Receiver Operating Characteristic (ROC) curves, which allowed expressing the Probability Of Detection (POD) function of the Probability of False Alarm (PFA) varying the threshold over which a structure was considered as damaged. Such criterion was chosen as it allows evaluating how much the algorithm is able to distinguish a damaged blade from a pristine blade, in fact, this is key aspect in the cost effectiveness of SHMS, which have to maximize the POD minimizing the PFA. ROC curves were derived for all the noise levels 1%, 2%, 4%, and 6%, for each damage dimension and considering all the three versions of the algorithm. Preliminary results suggested that the algorithm was not sensitive to small damages, as the related ROC curves were positioned on the no-performance line: the diagonal of the ROC plot that represents a random classifier. To improve the detection performances for high damage dimensions, since no performance was obtained with lower ones, the ANN 2 was trained excluding the damages with smaller size like 3 mm, 6 mm and 9 mm, as suggested in [33], maintaining the same dataset partition between pristine and damage cases. POD and PFA were calculated according to the "HIT/MISS data" method presented in [43]. POD was calculated considering damaged conditions and counting the number of times that the output of the ANN 2 exceeded the threshold value, this was then divided by the total number of damaged conditions analysed by the ANN 2, as reported in Eq. 7.

$$POD = \frac{TP}{TP+FN} \qquad (7)$$

Where TP represented the True Positives (damaged conditions classified as damaged) and FN represented the False Negatives (damaged conditions classified as pristine), their sum gave the total number of damaged conditions analysed by the *ANN 2*.

The PFA was calculated considering instead pristine conditions, the number of times that the output of the *ANN 2* exceeded the threshold value was divided by the total number of pristine conditions analysed by the *ANN 2*, as reported in Eq. 8.

$$PFA = \frac{FP}{FP+TN} \qquad (8)$$

Where TN represented the true negatives (pristine conditions classified as pristine) and FP represented the false positives (pristine conditions classified as damaged), their sum represented the total number of pristine configurations analysed by the *ANN 2*.

The ROC curves were then obtained calculating the POD and the PFA varying the threshold value from its minimum to its maximum value, in this specific case between 0 and 1.

In Figures 10–12 the ROC curves for version #1, version #2 and version #3 of the algorithm respectively are shown.

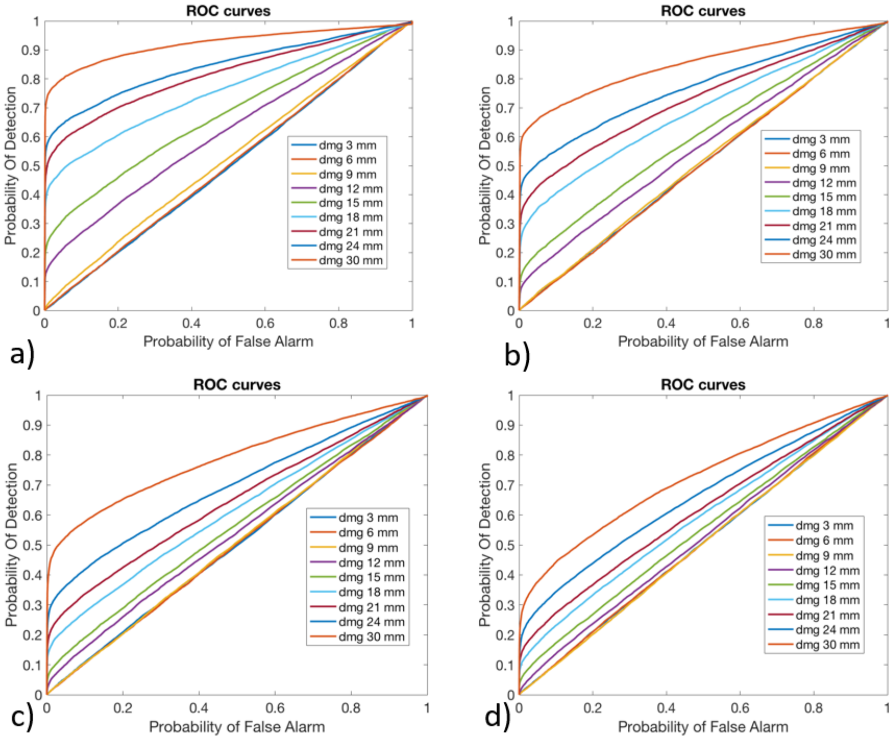

Figure 10. Receiver Operating Characteristic curves for algorithm version #1 obtained with a) 1% Gaussian noise, b) 2% Gaussian noise, c) 4% Gaussian noise and d) 6% Gaussian noise.

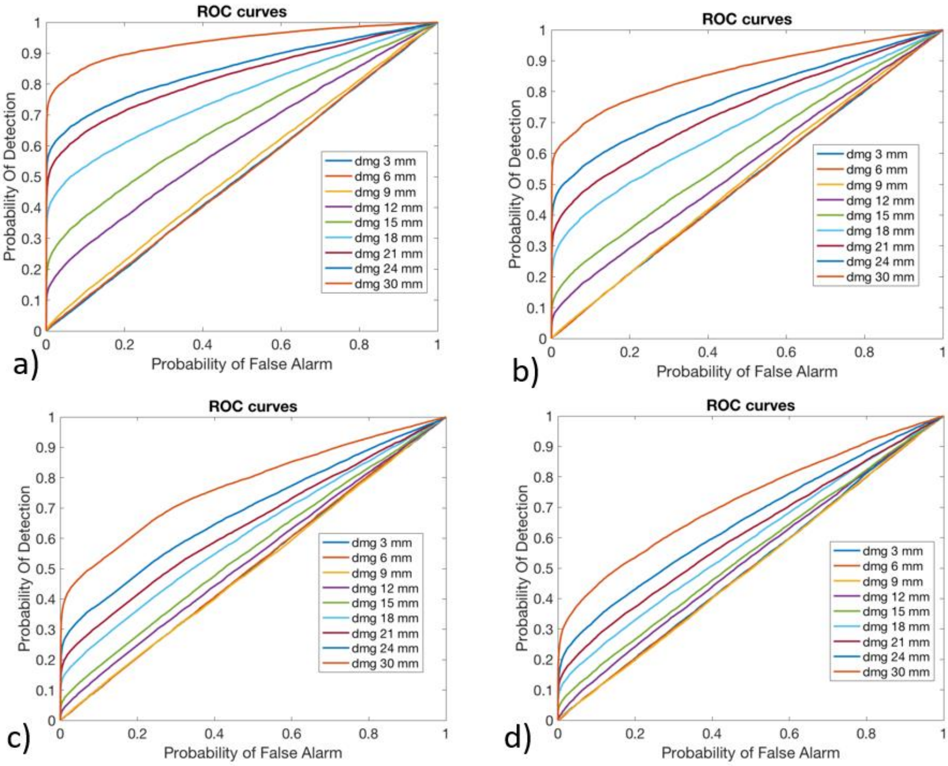

Figure 11. Receiver Operating Characteristic curves for algorithm version #2 obtained with a) 1% Gaussian noise, b) 2% Gaussian noise, c) 4% Gaussian noise and d) 6% Gaussian noise.

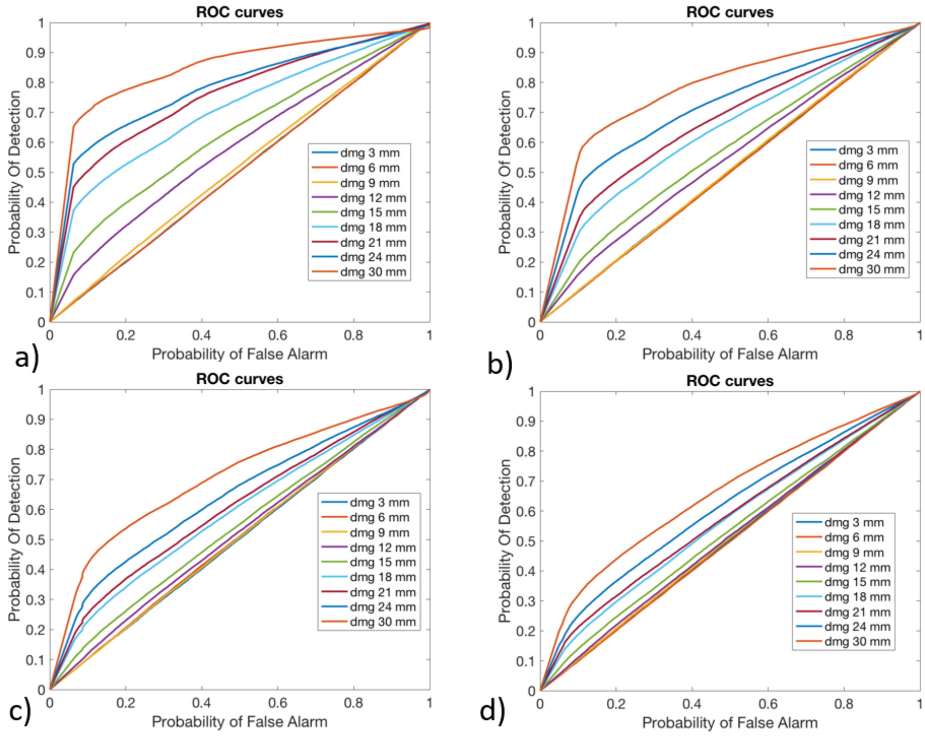

Figure 12. Receiver Operating Characteristic curves for algorithm version #3 obtained with a) 1% Gaussian noise, b) 2% Gaussian noise, c) 4% Gaussian noise and d) 6% Gaussian noise.

As it can be observed, damages with a higher dimension were more likely to be detected, being their curve in the upper-left side of the plot. Damages with lower dimensions like 3 mm, 6 mm and 9 mm could not be identified by anyone of the versions of the algorithm, being their curve on the no-performance line corresponding to segment connecting the axis origin to the point (1,1). As it was expected by increasing the level of noise the algorithm decreases its performances reducing the POD for the same PFA. Version #1 and version #2 of the algorithm seemed to provide comparable results in the anomaly detection, while version #3 of the algorithm provided significant lower performances.

In fact, especially for small value of PFA (where the optimal threshold should be chosen) the POD showed very small values compared to version #1 and version #2 of the algorithm.

4.3. Damage Assessment and Localization

Once the presence of damage was detected, the subsequent step was related to its assessment and localization. In fact, these two steps provided information useful for decision making. For instance, depending on the estimated damage size, a fast decision can be made about repairing or substituting the blade, without the needed to inspect the blade with NDT. The localization of the damage allows an automatic identification of its position, making possible the evaluation of the effects of the damage in that specific point of the structure.

The ANN 3 was trained only on damaged configurations: damage size and position were given together to the ANN 3 as preliminary studies revealed that no improvement would be obtained by using two different ANN for damage assessment and localization respectively. In Figure 13 the plot of the real damage size and the estimated damage size is shown for all of three versions of the algorithm and for each level of noise. The dashed line coloured in purple represented the theoretical behaviour that the algorithm should have, as its angular coefficient it's one it means that for each real damage size the algorithm should provide exactly that one. The more an algorithm has higher performances, the more its behaviour is similar to the theoretical behaviour.

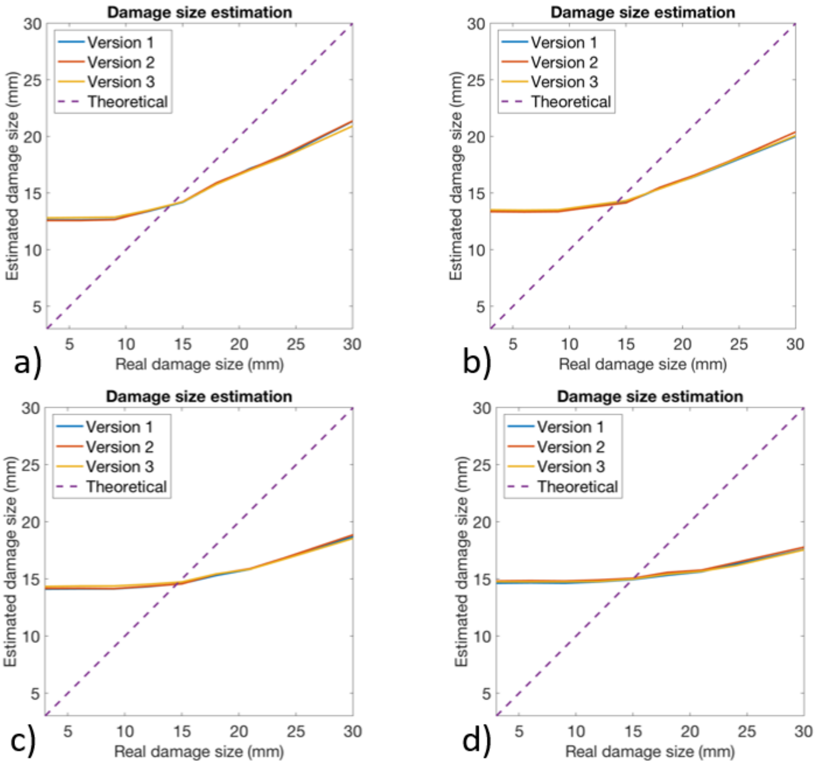

Figure 13. damage quantification obtained for all the three versions of the algorithm with a) 1% Gaussian noise, b) 2% Gaussian noise, c) 4% Gaussian noise and d) 6% Gaussian noise.

For damages with a reduced size, it can be seen that the algorithm overestimated the damage size maintaining an estimation of about 15 mm, such behaviour was observed for real damage size below 15 mm. As the real damage size increased above 15 mm the algorithm seemed to provide a more accurate estimation of the size of the damage, anyway, the behaviour was still far from the theoretical one. No significant difference existed between the three versions of the algorithm, it seemed that version #2 provided a little bit better results with respect to the others, however such difference seemed to be very low. The main factor affecting the performance of the algorithm was represented by the noise level: as the noise level increased the algorithm seemed to become less sensitive to the size of the damage. In particular, it was observed that the slope of the curves decreased as the noise level increased, moreover, it seemed that the noise affected at the same way all the versions of the algorithm. The low sensitivity to the damage size may be due to the relatively low effects that a damage in the adhesive produce. In fact, the central core was much stiffer than the antitorsional layer, therefore, a disbonding slightly affects the deformation field and, consequently, damage size estimation resulted to be difficult.

Performances about damage localization are presented in Figure 15 expressed in terms of mean percentage errors related to the cross section and curvilinear coordinates represented in Figure 7a. The percentage error was calculated considering, for each of the two coordinates, the absolute value of the difference between the real damage coordinate and the damage coordinate estimated by the ANN 3. The coordinates were already expressed in percentage of the total length.

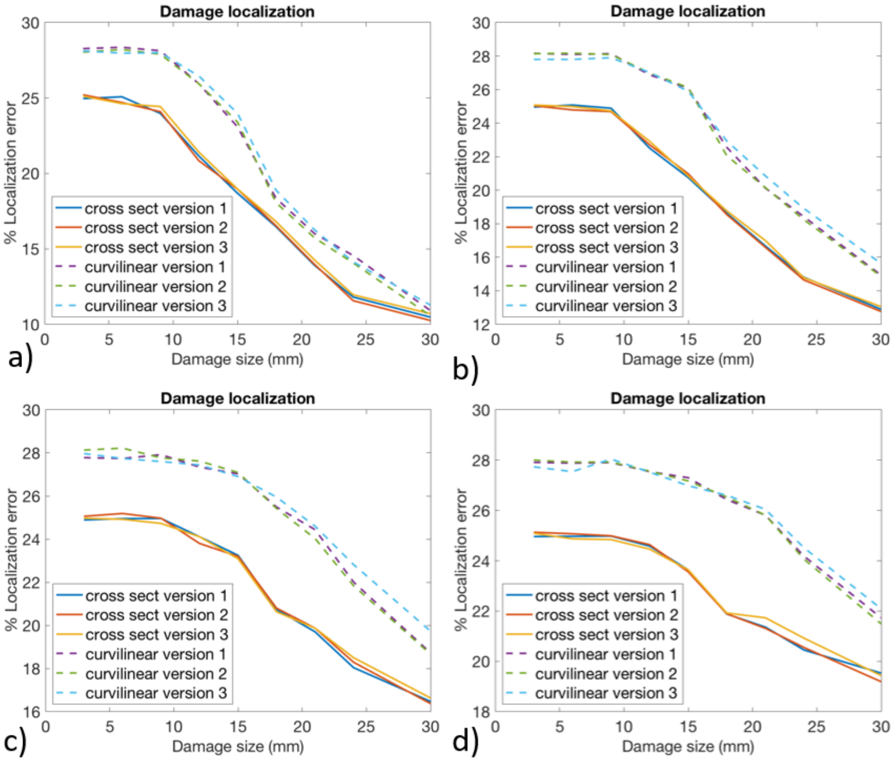

Figure 14. percentage error in damage localization obtained for all of three versions of the algorithm with a) 1% Gaussian noise, b) 2% Gaussian noise, c) 4% Gaussian noise and d) 6% Gaussian noise.

It was interesting to observe that for small damage dimensions the localization error for both the coordinates was slightly affected by the level of noise and it maintained a value of 28% and 25% for curvilinear and cross section coordinates respectively. Moreover, for small damage sizes the performances of all the versions of the algorithm seemed to be similar. As the dimension of the damage increased the error decreased for both the coordinates and the identified damage position seemed to provide lower performances as the noise level increased. In fact, it can be observed that for a damage size of 30 mm, the error for the cross section coordinate passed from 10-11% with a noise level of 1% to an error of 19% with a noise level of 6%. In general, no significant difference existed between the three versions of the algorithm, especially for low levels of noise, overall, version #3 seemed to provide slightly higher errors for what concern the curvilinear coordinate for higher level of noise, while version #1 and version #2 exhibited similar behaviour.

Figure 15 represents a comparison between the strain field distribution in a damaged and undamaged blade root. The elements represented are related to the ply containing the virtual optical fibres. Considering the size of the damage, which was in this case equal to 30 mm, it should be observed that the strain distribution was almost not affected by the presence of the damage.

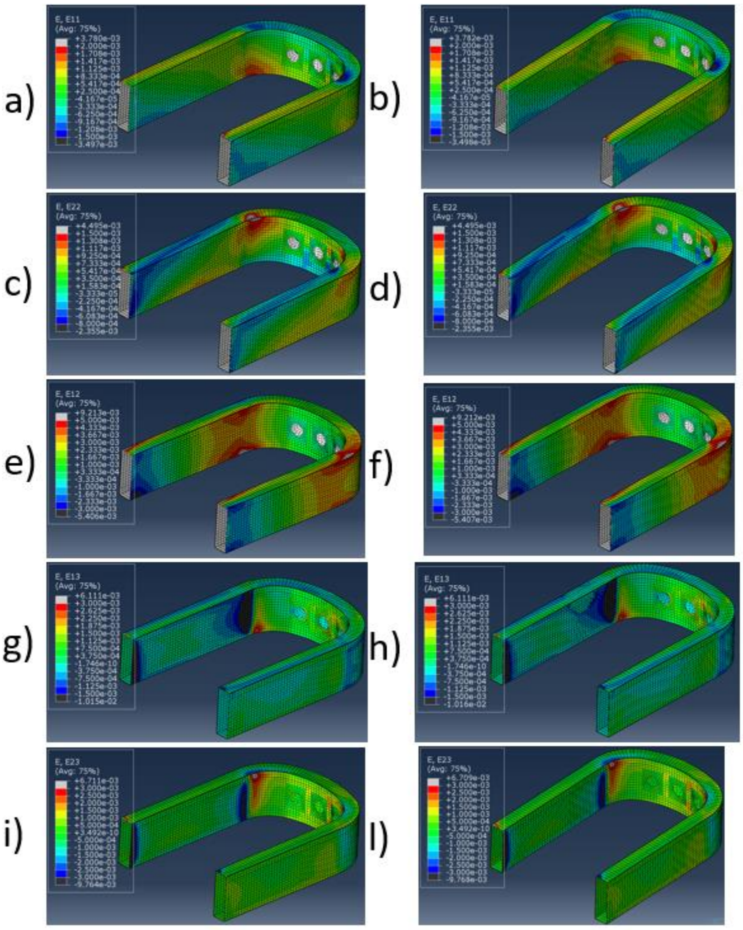

Figure 15. Strain field distribution in the elements local reference system of pristine blade root and damaged blade root with damage of 30 mm diameter located at 50% of cross-section coordinate and 22.22% of curvilinear path coordinate, a) ε_{11} pristine, b) ε_{11} damaged, c) ε_{22} pristine, d) ε_{22} damaged, e) γ_{12} pristine, f) γ_{12} damaged, g) γ_{13} pristine, h) γ_{13} damaged, i) γ_{23} pristine, l) γ_{23} damaged.

Only one strain component seemed to be influenced by the presence of the damage, which is represented in Figure 15h and it was the out of plane shear γ_{13}: however, such strain component is particularly difficult to be measured with an FBG sensor, as they are sensitive to the deformation along the optical fibre path.

5. Conclusions

The performances of a SHMS were evaluated on a composite rotor blade root subjected to a variable loading condition. The component was modelled with FE and the elements located on the path of the virtual optical fibres were supposed providing the strain read by the FBG sensors. The FE model was previously validated with experiments loading the blade root in a test rig and applying seven different loads representative of the real operational conditions. Damages of different dimensions and in different positions were introduced in the adhesive layer between the central core and the anti-torsional layer, an algorithm based on ANN was proposed to identify the presence of damages under variable loading conditions. Three different versions of the algorithm, that differed in the way the load set was identified, were compared in terms of damage detection performances. The load set identification, obtained with the solution of the inverse problem (version #3), was found to be particularly critical, as the load set was identified with a poor quality. Moreover, two loads of the load set were identified with an error of five to twenty times the maximum magnitude reached by that loads. The usage of the ANN 1 to recognize the load set revealed to be particularly effective compared to solving the inverse problem as the error reduced by one order of magnitude. The quality of the identified loads in a damaged blade seemed to be worse with respect to the one obtained with the blade in pristine conditions, however such difference seemed to become negligible by increasing the level of noise. For what concerns the anomaly detection the ANN 2 was trained on a dataset made of half pristine and half damaged conditions, it was found that especially in this step the quality in the identification of the load set was particularly relevant, for example, the identified load set with version #1 and version #2 of the algorithm provided reasonable values of POD for small values of PFA. This behaviour actually was not observed when the loads were identified solving the inverse problem with version #3, as the same POD was reached for higher values of PFA. ANN 3 was trained only on damaged conditions and its objective was to identify the damage size together with its location, as preliminary studies suggested that no benefit would be obtained using two different ANN for the damage assessment and localization. Damage assessment was found to be effective for damage sizes higher than 15 mm, as for lower damage dimensions the output of the ANN 3 was maintained at a constant value. All the three versions of the algorithm provided similar results in terms of performances and a high sensitivity to noise was found. For what concerns the localization of the damage, version #3 of the algorithm provided higher error with respect to the others for the curvilinear coordinate, even if such gap was less than 1%, while for the cross section coordinate all of the three versions exhibited similar performances passing from an error of about 10 % to an error of 19% for 1% noise level and 6% noise level respectively for a damage of size 30 mm. Overall, version #1 and version #2 of the algorithm showed similar behaviour while version #3 exhibited lower performances with respect to the others, this aspect was found to be particularly relevant in the anomaly detection step. It was found that including damaged conditions in the training of ANN 1 did not provide any benefit, especially if the level of noise is high, as the perturbation to the strain field created by the presence of the damage seemed to be covered by the effect of the noise. The strain field of the anti-torsional ply in correspondence of the virtual sensors was analysed with a FE model considering the most relevant strain components and it was found that the effect of a damage of 30 mm, which was the maximum size considered in this study, generated very little effects on the strain field, in particular, only the out of plane shear strain seems to be influenced, which was however not captured by the sensors. This result should be understandable, in fact, considering that the core of the cross section was much stiffer with respect to the anti-torsional layer, the influence of the damage on the total stiffness resulted to be low, thus limiting the possibility of a damage to be identified.

This work was limited to the hypothesis of model linearity. However, the contact interactions between the blade root and the bearing represented a source of nonlinearity. Future works will be needed to validate the performance of the algorithm with experimental tests, especially to evaluate the effects of the nonlinearity of the problem. Moreover, experiments should be performed to assess the modelling of the damage, which in this work was addressed deleting the cohesive elements of the adhesive layer. Despite the large number of FBG sensors contributing to cost increase; a cost-benefit analysis needs to be performed to evaluate the economic impact of the SHMS on the lifecycle of the blade.

Author Contributions: Conceptualization, Pietro Ballarin and Alessandro Airoldi; methodology, Pietro Ballarin and Alessandro Airoldi; validation, Andrea Baldi; formal analysis, Pietro Ballarin; investigation, Pietro Ballarin, Alessandro Airoldi, Andrea Baldi; resources, Andrea Baldi; data curation, Pietro Ballarin and Andrea Baldi; writing—original draft preparation, Pietro Ballarin and Alessandro Airoldi; writing—review and editing, Alessandro Airoldi, Andrea Baldi, Marco Macchi, Irene Roda, Giuseppe Sala; supervision, Alessandro Airoldi, Giuseppe Sala; project administration, Alessandro Airoldi, Giuseppe Sala. All authors have read and agreed to the published version of the manuscript.

Funding: This research received no external funding.

Data Availability Statement: The data presented in this study are available on request from the corresponding author due to confidentiality restriction.

Conflicts of Interest: The authors declare no conflicts of interest.

References

1. Hassan M H (2021) A mini review on manufacturing defects and performance assessments of complex shape prepreg-based composites. The international Journal of Advanced Manufacturing Technology, 115:3393-3408.
2. Hallander P, Akermo M, Mattei C, Petersson M, Nyman T (2013) An experimental study of mechanisms behind wrinkle development during forming of composite laminates. Composites Part A, 50:54-64.
3. Yerramalli C S, Miebach T, Chandraseker K, Quek S C (2010) Fiber waviness induced knockdowns in composite materials used in wind turbine blades. Conference paper: European Wind Energy Conference and Exhibition 2010.
4. Bloom L D, Wang J, Potter K D (2013) Damage progression and defect sensitivity: An experimental study of representative wrinkles in tension. Composites Part B, 45: 449-458.
5. Hakim I, Laquai R, Walter D, Mueller B, Graja P, Meyendorf N, Donaldson S (2017) The effect of manufacturing conditions on discontinuity population and fatigue fracture behavior in carbon/epoxy composites. Conference paper: AIP Conf. Proc. 1806, 090017-1-090017-11, Atlanta, 2017.
6. Suhot M A, Chambers A E (2007) The effect of voids on the flexural fatigue performace of unidirectional carbon fibre composites. Conference paper: 16th International conference on composite materials, Kyoto, 2007.
7. Lightfoot J S, Wisnom M R, Potter K (2013) A new mechanism for the formation of ply wrinkles due to shear between plies. Composites Part A, 49:139-147.
8. Boisse P, Hamila N, Vidal-Sallé E, Dumont F (2011) Simulation of wrinkling during textile composite forming. Influence of tensile, in-plane shear and bending stiffness. Composites Science and Technology, 71:683- 692.
9. Mujahid Y, Sallih N, Abdullah M Z, Mustapha (2020) Effects of processing parameters for vacuum-bag-only method on void content and mechanical properties of laminated composites. Polymer Composites, 42:567-582.
10. Grunenfelder L K, Nutt S R (2010) Void formation in composite prepregs - Effect of dissolved moisture. Composites Science and Technology, 70:2304-2309.
11. Zhang T, Meng J, Pan Q, Sun B (2019) The influence of adhesive porosity on composite joints. Composite Communications, 15:87-91.
12. Malinowski P H, Wandowski T, Ostachowicz W M, Christopoulos A, Koulalis I, Kitsianos K, ... & Brune K (2018). Study of CFRP adhesive bonds influenced by manufacturing-related contaminations. Sensors and Smart Structures Technologies for Civil, Mechanical, and Aerospace Systems 2018 (Vol. 10598, p. 105980B). International Society for Optics and Photonics.
13. Moutsompegka E, Tserpes K I, Polydoropoulou P, Tornow C, Schlag M, Brune K, Mayer B, Pantelakis S (2017) Experimental study of the effect of pre-bond contamination with de-icing fluid and ageing on the fracture toughness of composite bonded joints. Fatigue of aeronautical materials & structures, 40:1581-1591.
14. Markatos D N, Tserpes K I, Rau E, Markus S, Ehrhart B, Pantelakis S (2013) The effects of manufacturing-induced and in-service related bonding quality reduction on the mode-I fracture toughness of composite bonded joints for aeronautical use. Composites Part B, 45:556-564
15. Solodov I, Segur D, Kreutzbruck M (2018) Evaluation of bonding quality in CFRP composite laminates by measurements local vibration nonlinearity. Conference paper: DGZfP-Jahrestagugng 2018 Leipzig.
16. Yılmaz B, Jasiuniene E (2020) Advanced ultrasonic NDT for weak bond detection in composite-adhesive bonded structures. International Journal of Adhesion and Adhesive, 102, 102675.
17. Wang, B., Zhong, S., Lee, T. L., Fancey, K. S., & Mi, J. (2020). Non-destructive testing and evaluation of composite materials/structures: A state-of-the-art review. Advances in mechanical engineering, 12(4), 1687814020913761.
18. Gholizadeh, S. (2016). A review of non-destructive testing methods of composite materials. Procedia structural integrity, 1, 50-57.
19. Jolly, M. R., Prabhakar, A., Sturzu, B., Hollstein, K., Singh, R., Thomas, S., ... & Shaw, A. (2015). Review of non-destructive testing (NDT) techniques and their applicability to thick walled composites. Procedia CIRP, 38, 129-136.
20. Boller, C. (2001). Ways and options for aircraft structural health management. Smart materials and structures, 10(3), 432.
21. Speckmann, H., & Henrich, R. (2004, August). Structural health monitoring (SHM)–overview on technologies under development. In Proceedings of the 16th World Conference on NDT (Vol. 1)
22. Rocha, H., Semprimoschnig, C., & Nunes, J. P. (2021). Sensors for process and structural health monitoring of aerospace composites: A review. Engineering Structures, 237, 112231
23. Dong, T., & Kim, N. H. (2018). Cost-effectiveness of structural health monitoring in fuselage maintenance of the civil aviation industry. Aerospace, 5(3), 87.
24. Takeda, N., Okabe, Y., Kuwahara, J., Kojima, S., & Ogisu, T. (2005). Development of smart composite structures with small-diameter fiber Bragg grating sensors for damage detection: Quantitative evaluation

of delamination length in CFRP laminates using Lamb wave sensing. Composites science and technology, 65(15-16), 2575-2587.

25. Ghiasvand, S., Airoldi, A., Bettini, P., & Mirani, C. (2022). Analysis of residual stresses and interface damage propagation in hybrid composite/metallic elements monitored through optical fiber sensors. Aerospace Science and Technology, 107373.
26. Goossens, S., De Pauw, B., Geernaert, T., Salmanpour, M. S., Khodaei, Z. S., Karachalios, E., ... & Berghmans, F. (2019). Aerospace-grade surface mounted optical fibre strain sensor for structural health monitoring on composite structures evaluated against in-flight conditions. Smart Materials and Structures, 28(6), 065008.
27. Mieloszyk, M., Skarbek, L., Krawczuk, M., Ostachowicz, W., & Zak, A. (2011). Application of fibre Bragg grating sensors for structural health monitoring of an adaptive wing. Smart Materials and Structures, 20(12), 125014.
28. Di Sante, R. (2015). Fibre optic sensors for structural health monitoring of aircraft composite structures: Recent advances and applications. Sensors, 15(8), 18666-18713.
29. Loutas, T. H., Charlaftis, P., Airoldi, A., Bettini, P., Koimtzoglou, C., & Kostopoulos, V. (2015). Reliability of strain monitoring of composite structures via the use of optical fiber ribbon tapes for structural health monitoring purposes. Composite Structures, 134, 762-771.
30. Gardner, P., Fuentes, R., Dervilis, N., Mineo, C., Pierce, S. G., Cross, E. J., & Worden, K. (2020). Machine learning at the interface of structural health monitoring and non-destructive evaluation. Philosophical Transactions of the Royal Society A, 378(2182), 20190581.
31. Fakih, M. A., Chiachío, M., Chiachío, J., & Mustapha, S. (2022). A Bayesian approach for damage assessment in welded structures using Lamb-wave surrogate models and minimal sensing. NDT & E International, 128, 102626.
32. Sbarufatti, C., Manes, A., & Giglio, M. (2011). Sensor network optimization for damage detection on aluminium stiffened helicopter panels. In COUPLED IV: proceedings of the IV International Conference on Computational Methods for Coupled Problems in Science and Engineering (pp. 1294-1305). CIMNE.
33. Sbarufatti, C., Manes, A., & Giglio, M. (2013). Performance optimization of a diagnostic system based upon a simulated strain field for fatigue damage characterization. Mechanical Systems and Signal Processing, 40(2), 667-690.
34. Alvarez-Montoya, J., Torres-Arredondo, M., & Sierra-Pérez, J. (2018). Gaussian process modeling for damage detection in composite aerospace structures by using discrete strain measurements. In Proceedings of the 7th Asia-Pacific Workshop on Structural Health Monitoring, APWSHM 2018 (pp. 710-8).
35. Sierra-Pérez, J., Torres-Arredondo, M. A., & Alvarez-Montoya, J. (2017). Damage detection methodology under variable load conditions based on strain field pattern recognition using FBGs, nonlinear principal component analysis, and clustering techniques. Smart Materials and Structures, 27(1), 015002.
36. Alvarez-Montoya, J., Carvajal-Castrillón, A., & Sierra-Pérez, J. (2020). In-flight and wireless damage detection in a UAV composite wing using fiber optic sensors and strain field pattern recognition. Mechanical Systems and Signal Processing, 136, 106526.
37. Lin, M., Guo, S., He, S., Li, W., & Yang, D. (2022). Structure health monitoring of a composite wing based on flight load and strain data using deep learning method. Composite Structures, 286, 115305.[38] Dassault Systemes Simulia Corporation (2022). Abaqus Analysis User Maual Version 6.14
38. Turon, A., Davila, C. G., Camanho, P. P., & Costa, J. (2007). An engineering solution for mesh size effects in the simulation of delamination using cohesive zone models. Engineering fracture mechanics, 74(10), 1665-1682.
39. Anders Rytter, Vibrational Based Inspection of Civil Engineering Structures, PhD thesis, Department of Building Technology and Structural Engineering, Aalborg University, 1993.
40. Airoldi A, Marelli L, Bettini P, Sala G, Apicella A. Strain field reconstruction on composite spars based on the identification of equivalent load conditions. In: Proceedings of SPIE - The International Society for Optical Engineering. Vol 10168; 2017. https://doi.org/10.1117/12. 2260161
41. Zhang, M., Sun, Q., Wang, Z., Li, X., Liu, H., & Liu, D. (2012). A large capacity sensing network with identical weak fiber Bragg gratings multiplexing. Optics Communications, 285(13-14), 3082-3087.
42. Bottasso, L. M., Sala, G., Bettini, P., Tagliabue, P., Corbani, F., Platini, E., ... & Anelli, A. (2018). Rugged Fiber Optics Monitoring System for Helicopter Rotor Blades. In 44th European Rotorcraft Forum (ERF 2018) (pp. 965-980). Curran Associates.
43. Annis, C. (2007). Department of Defense Handbook: Nondestructive Evaluation System Reliability Assessment. MIL-HDBK-1823, United States Department of Defense.